Connectome modulates critical brain dynamics across local and global scales

Giovanni Rabuffo[1,*,†] Pietro Bozzo[2] Bach Nguyen[3] Damien Depannemaecker[2] Marco N. Pompili[2] Leonardo L. Gollo[4,5] Tomoki Fukai[3] Pierpaolo Sorrentino[2,6] and Leonardo Dalla Porta[7,*,‡]

[1]*Center for Brain and Cognition, Pompeu Fabra University, Barcelona, Spain*
[2]*Institute of System Neuroscience, Aix-Marseille University, Marseille, France*
[3]*Okinawa Institute for Science and Technology, Okinawa, Japan*
[4]*Institute for Cross-Disciplinary Physics and Complex Systems, IFISC (UIB–CSIC), University of the Balearic Islands, Palma de Mallorca, Spain*
[5]*Brain Networks and Modelling Laboratory, Monash University, Melbourne, Australia*
[6]*Department of Biomedical Sciences, University of Sassari, Sassari, Italy*
[7]*Institute of Biomedical Research August Pi i Sunyer (IDIBAPS), Barcelona, Spain*

(Received 17 December 2025; accepted 15 October 2026; published 17 November 2026)

Neuronal activity in the brain has been hypothesized to operate near criticality, a dynamical regime poised between order and disorder that maximizes information processing, adaptability, and dynamic range. While criticality has been extensively studied at local scales (within neuronal populations) and at global scales (across interacting brain regions), the interplay between these levels remains poorly understood. Here, we propose a multiscale computational framework that bridges *local* and *global* criticality within a single, mechanistic model. At the mesoscopic level, individual brain regions are represented by neural mass models tuned near the transition between asynchronous and synchronous regimes. These regions are then coupled via an empirically derived mouse connectome to investigate how structural connectivity shapes the emergence of large-scale coordination. We show that (1) local near-critical dynamics for an isolated brain region can be faithfully reproduced within a mean-field model framework, (2) local distance to criticality is modulated by long-range coupling, (3) whole-brain simulations reveal nonlinear gradients of timescales and heterogeneous shifts toward/away from local criticality, and (4) global criticality, manifested in scale-free avalanche distributions and optimal functional connectivity, emerges when local populations are locally tuned near criticality and coupled within an optimal range, a result that we confirm in whole-brain simulations of connectome-coupled spiking neurons. These results demonstrate that local and global criticality are dynamically intertwined but not directly aligned, and that their relationship depends on the underlying structural connectivity. Our multiscale modeling framework provides a tractable tool for generating testable hypotheses on how brain criticality co-arises across scales and how it may be modulated in health and disease.

DOI: 10.1103/n87d-5krk

I. INTRODUCTION

The concept of brain criticality (that the brain operates near a phase transition between order and disorder) has become a central framework in theoretical and empirical neuroscience [1–5]. At a critical point, neuronal activity exhibits long-range correlations [6], scale-free avalanches [7], and optimal computational properties such as maximal dynamic range and information transmission [8–10]. Evidence for critical-like behavior has been found both in local regions [7,11], where it emerges from the interactions among neurons within a cortical patch or microcircuit, and at the global scale [12–19], where it reflects coordination between distant brain regions (for a recent review, see Ref. [5]). Yet, these two levels of description have largely been studied separately.

From a theoretical standpoint, scale invariance suggests that the same principles could govern dynamics across spatial scales [20]. However, many brain features are specific to a particular scale, as opposed to being scale-free [21,22]: Distinct structural features characterize different levels, from dense, recurrent microcircuits to sparse, heterogeneous long-range connections. As a result, criticality may not simply "propagate" across scales. Local circuits tuned near criticality might not imply criticality at the whole-brain level, and conversely, large-scale coordination may emerge even when local dynamics deviate from criticality. Understanding this multiscale relationship is key to linking cellular and systems-level theories of brain function.

Here, we develop a multiscale modeling formalism to study local and global criticality at once [Fig. 1(a)]. At the mesoscopic level, each brain region is described by an all-to-all coupled network of "active rotator" neurons [23], which

*These authors contributed equally to this work.
†Contact author: giovanni.rabuffo@upf.edu
‡Contact author: dallaporta@recerca.clinic.cat

Published by the American Physical Society under the terms of the Creative Commons Attribution 4.0 International license. Further distribution of this work must maintain attribution to the author(s) and the published article's title, journal citation, and DOI.

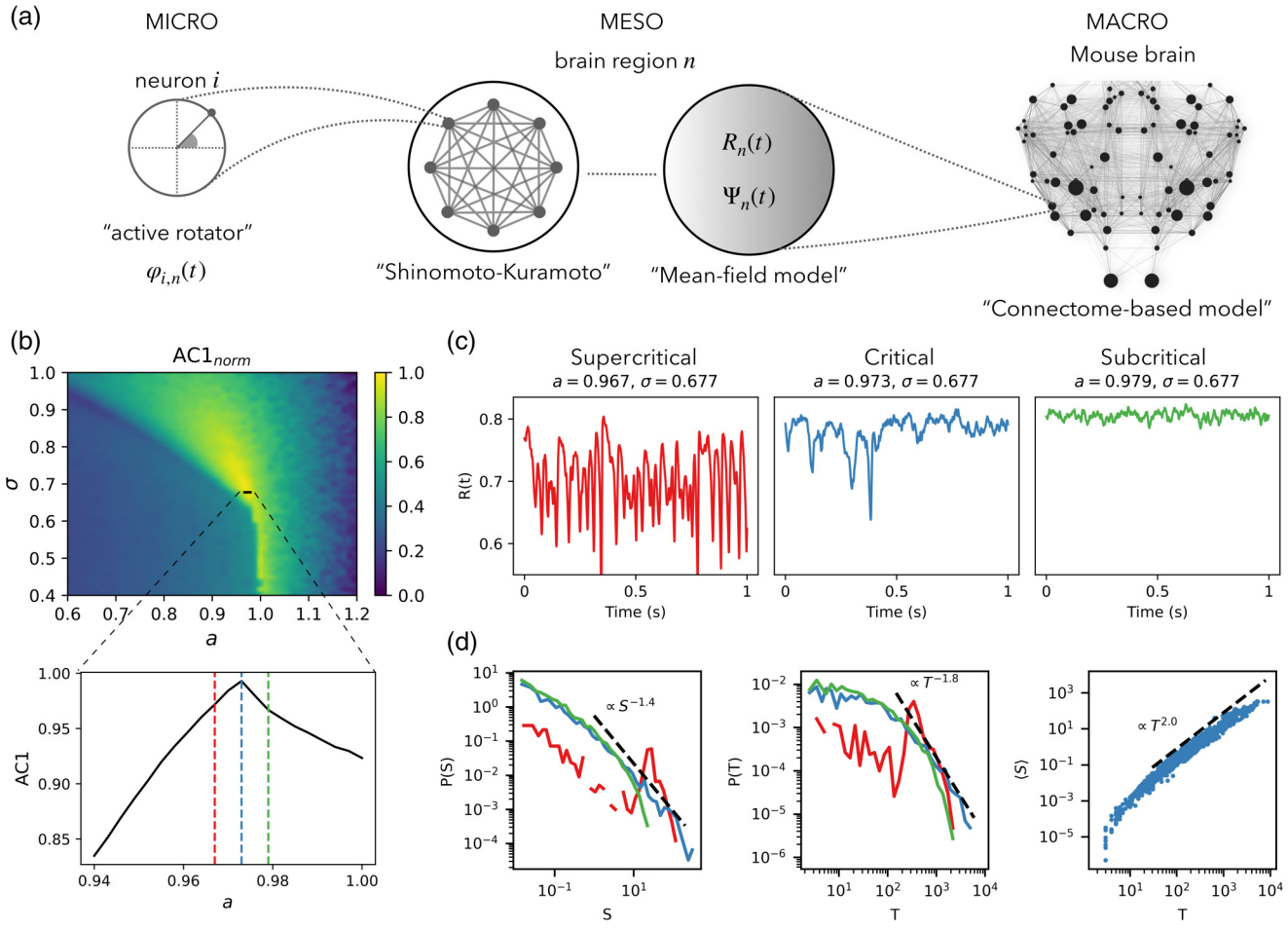


FIG. 1. Multiscale modeling and criticality analysis of brain region dynamics. (a) Schematic of the multiscale framework. At the microscale, each neuron i in the brain region n is modeled as an active rotator $\varphi_{i,n}(t)$. At the mesoscale, the collective dynamics are described by the Shinomoto-Kuramoto model for a population of all-to-all connected active rotators. This model admits a mean-field description, which reduces the neuronal population dynamics to only two equations for the mesoscopic variables $(R_n(t), \Psi_n(t))$. When driven by Gaussian noise of standard deviation $N = 0.0001$, the mean-field model describes the activity of an isolated brain region. At the macroscale, brain regions are coupled according to a mouse connectome from the Allen Institute [26]. (b) Exploration of the local model's parameter space. The heatmap shows the normalized autocorrelation at lag 1 ms (AC1) of $R(t)$ over different values of the coupling parameter a and noise amplitude σ, revealing a ridge of critical-like dynamics. A close-up along $\sigma = 0.677$ highlights representative supercritical (red; $a = 0.967$), critical (blue; $a = 0.973$), and subcritical (green; $a = 0.979$) regimes, consistent with microscopic network simulations [24]. (c) Example time series of $R(t)$ in each near-critical regime. (d) Avalanche analysis: Avalanches are defined as consecutive time points where $R(t)$ falls below its median value. Shown are distributions of avalanche sizes S [the area between $R(t)$ and the threshold over the event] and durations T (number of time steps of the event), as well as the scaling of size S vs duration T in the critical regime. Dashed lines mark the exponents fitted in the critical regime, $P(S) \propto S^{-1.4}$, $P(T) \propto T^{-1.8}$, and $S \propto T^{2.0}$, which satisfy the crackling-noise relation $(\alpha - 1)/(\tau - 1) \approx \gamma$; a power law is preferred over an exponential distribution only in the critical regime (Sec. IV).

reproduces subcritical, critical, and supercritical regimes [24]. This network admits an analytic mean-field reduction [24,25], allowing us to systematically characterize regional dynamics and their dependence on local parameters. At the macroscopic level, distinct brain regions are coupled according to a mouse structural connectome [26,27], enabling us to study how anatomical connectivity shapes large-scale coordination and modulates each region's proximity to criticality.

We first show that, using only two coupled, noise-driven variables, the local neural mass model reproduces hallmark signatures of criticality, including increased temporal correlations and scale-free avalanche statistics. We then investigate how long-range coupling between regions in different regimes can shift the dynamics of the downstream region toward or away from criticality, revealing nontrivial cross-regime influences. Extending to whole-brain simulations, we show that global coupling systematically modulates local regimes according to the region-specific connectivity, giving rise to topological gradients of timescales whose direction depends on whether regions are tuned to subcritical, critical, or supercritical states. Crucially, we find that global criticality [reflected in large-scale avalanche scaling and optimal fit to empirical functional connectivity (FC)] emerges when all local populations are tuned near criticality and weakly coupled.

These results advance a unifying view in which local and global criticality are not independent phenomena but

dynamically coupled aspects of brain organization. By embedding minimal models of local dynamics into a realistic connectome, our approach bridges levels of description and provides a tractable test bed for investigating how structural connectivity and dynamical tuning interact to shape multiscale coordination. Beyond its theoretical significance, this framework offers concrete hypotheses for experimental probing of criticality across scales, and may help explain how pathological alterations in local or global dynamics disrupt brain function.

II. RESULTS

A. A mean-field description of local critical dynamics

We first investigated whether a reduced mean-field model formulation could reproduce the critical-like dynamics observed in detailed neuronal network models. We modeled each isolated brain region as the mean-field limit of an all-to-all connected population of active rotators [24,25], retaining the key Kuramoto mesoscopic variables ($R_n(t)$, $\Psi_n(t)$), representing the population's synchronization and average phase, while achieving a substantial reduction in dimensionality [Fig. 1(a)]. Adding stochastic noise and exploring the model parameters, including the network excitability a and the noise amplitude σ, we generated nontrivial mean-field dynamics for a population of neurons (see Figs. S1(a) and S1(b) in the Supplemental Material (SM) [28]).

Near a critical point, neural populations exhibit critical slowing down, meaning that perturbations decay more slowly and activity becomes increasingly temporally correlated [29]. This makes short-lag autocorrelation a sensitive indicator of proximity to criticality [30]. Accordingly, we quantified temporal structure using the autocorrelation function at a 1-ms delay (AC1). Systematic exploration of the parameter space revealed a ridge of critical-like dynamics, where AC1 is maximized [Figs. 1(b) and 1(c), blue].

Moving from this critical regime, fixing $\sigma = 0.677$ and decreasing the parameter a produces oscillatory dynamics, corresponding to a supercritical regime with highly synchronous neuronal activations [Figs. 1(b) and 1(c), red]. Conversely, increasing a leads to a subcritical regime with asynchronous, low-activity dynamics [Figs. 1(b) and 1(c), green]. Note that in the latter case, the Kuramoto order parameter $R(t)$ remains high, as a result of prolonged silent periods, reflecting synchrony in weak neuronal activity (Fig. S2 in SM [28]). Neural network simulations by Buendia and colleagues show a similar phase diagram for a network of all-to-all connected active rotators (see the hybrid-type (HT) regimes in Fig. 3 of Ref. [24]). The authors demonstrate diverse bifurcation points between synchronous and asynchronous states, with the critical regime corresponding to an HT transition, where incipient oscillations coexist with an asynchronous state. Running deterministic simulations, we confirmed the existence of bistability in the mean-field model for the parameters that maximize the AC1 (Fig. S1(c) in SM [28]).

Avalanche analyses confirmed that, at the HT transition, the mean-field model reproduces scale-free avalanche size and duration statistics consistent with critical dynamics [Fig. 1(d)]. Together, the AC1 ridge [Figs. 1(b) and 1(c)], the coexistence of attractors in the deterministic mean field at the same (a, σ) location (Fig. S1(c) in SM [28]), and the scale-free avalanche statistics [Fig. 1(d)] consistently identify this operating point as the hybrid-type bifurcation of Ref. [24], and rule out alternatives such as a Hopf bifurcation (locally unique) or a saddle-node-on-invariant-circle (SNIC) bifurcation (single attractor at the saddle node), neither of which is compatible with the observed bistability. These results validate the minimal model as a useful representation of near-critical local neuronal population dynamics, suitable for large-scale coupling in connectome-based simulations. Throughout, we refer to this hybrid-type transition point as the *critical* regime, and in the coupled networks we complement AC1 with further indicators of criticality, namely, the detrended fluctuation analysis (DFA) scaling exponent, the susceptibility, and avalanche statistics.

B. Cross-regime coupling can shift local dynamics toward or away from criticality

To examine the mechanistic basis of how long-range coupling influences local regimes, we simulated unidirectionally connected pairs of brain regions A (source) and B (target), exploring the (a_A, a_B) parameters systematically. Depending on the initial dynamical states, the activity in the target region varied. For example, when a supercritical source was coupled to a subcritical target [Figs. 2(a) and 2(b)], or vice versa [Figs. 2(c) and 2(d)], the target region shifted toward the critical regime. Coupling two critical brain regions did not alter the dynamical state of the target, preserving criticality [Figs. 2(e) and 2(f)]. Conversely, coupling a subcritical source to a critical or subcritical target further increased the target's distance from criticality (not shown). These results are summarized in Fig. 2(g), reporting the normalized difference ΔAC1 between AC1 of population B in coupled versus uncoupled cases. Increased or decreased AC1 marks an approach to or a distancing from criticality, respectively. This interpretation follows directly from the single-population results [Fig. 1(b)], where AC1 exhibited a pronounced peak along the critical ridge. There, the maximized short-lag autocorrelation reflected critical slowing down, providing a sensitive indicator of proximity to the transition. By analogy, changes in AC1 in the coupled-population model can therefore be taken as shifts toward or away from this critical regime. When the populations are mutually coupled with feedback loops [Fig. 2(h)], results are comparable to the only feedforward case and differ mostly when the upstream population dwells around a critical state [Fig. 2(i)], demonstrating higher sensitivity in these regimes. The same qualitative effects are observed when the two regions are simulated as coupled networks of 5000 spiking neurons each, tuned around the hybrid-type transition of the spiking model (Fig. S14 in SM [28]; since the spiking and mean-field parameter spaces do not map one-to-one, the spiking populations are placed relative to their own transition): Contrasting source and target regimes bring the target closer to the transition, a subcritical source pushes a critical target away from it, and feedforward coupling between two critical regions leaves the target near the transition. In the spiking network, mutual coupling between two critical regions

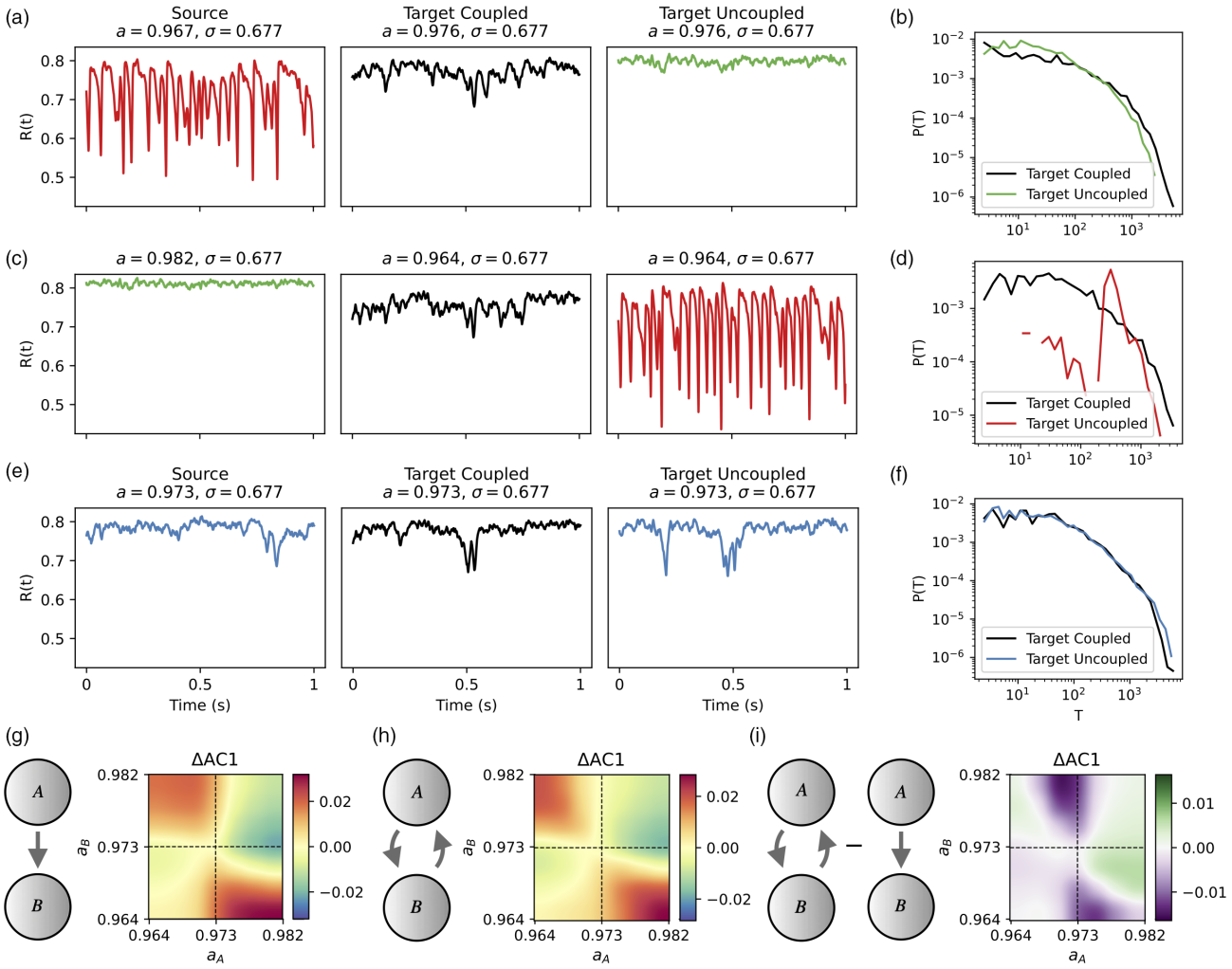


FIG. 2. Coupling between brain regions modulates criticality in the target. (a)–(f) Two mesoscopic populations, A (source) and B (target), are coupled unidirectionally. We fix the parameter $\sigma = 0.677$ as in Fig. 1, and the global coupling to $G = 0.05$ (for details on the coupling function, refer to Sec. IV). We systematically vary the parameters (a_A, a_B) of each region to place them in supercritical, critical, or subcritical regimes, and assess the effect of coupling on the target population B. Example time series and avalanche distributions for three representative cases [avalanches are excursions of $R(t)$ below its median, characterized by their duration T, the number of time steps of each excursion]: (a), (b) supercritical source to subcritical target, (c), (d) subcritical source to supercritical target, and (e), (f) critical-to-critical coupling. In each case, coupling alters the target dynamics and modifies its avalanche statistics, often enhancing scale-free properties near criticality. (g) Heatmaps show the relative change of AC1 computed on the target's dynamics [defined as $\Delta\mathrm{AC1} = (\mathrm{AC1}_{\mathrm{B,coupled}} - \mathrm{AC1}_{\mathrm{B,uncoupled}})/\mathrm{AC1}_{\mathrm{B,uncoupled}}$]. The results demonstrate that cross-regime coupling can induce nontrivial effects, often driving the target closer to criticality when source and target begin in contrasting dynamical states (e.g., supercritical → subcritical, or vice versa). (h) Similar to panel (g), for mutually coupled populations. (i) Relative difference between panels (h) and (g).

drives both across the transition, consistent with the higher sensitivity of the critical regime to feedback noted above. In summary, the long-range coupling can alter the local dynamical regime of a brain region, promoting or disfavoring critical dynamics.

C. Critical local tuning best matches empirical FC and dFC at intermediate coupling

We simulated whole-brain dynamics by coupling neural mass models through the directed structural connectivity of the Allen Mouse Brain Atlas [26,27]. Each brain region is represented as a network node, and nodes are initialized homogeneously in one of three dynamical regimes (subcritical, critical, or supercritical) depending on the choice of local parameters (i.e., keeping $\sigma = 0.677$ fixed, and using the three values of parameter a as in Fig. 1). The coupling strength between regions is controlled by a global parameter G, which scales the influence of long-range connectivity on local dynamics: For $G = 0$, regions evolve independently, while increasing G progressively introduces interregional interactions. In the next sections, we investigate the results of whole-brain simulations at two levels: (1) using the fast neuroelectric signals at 2000 Hz (i.e., the same type of signal analyzed in the previous sections); and (2) using the slow blood-oxygen-level-dependent (BOLD) signals at 1 Hz,

obtained by applying a Balloon-Windkessel hemodynamic response function to the neuroelectric signals.

First, to ground our simulations to empirical data, we compared the simulated BOLD activity with resting-state functional magnetic resonance imaging (fMRI) recordings from 53 control mice under light anesthesia [Fig. 3(a)]. For each mouse recording, we evaluated model performance by comparing simulated and empirical FC and dynamic FC (dFC) statistics across a range of G [Fig. 3(b)]. For all three local regimes, an appropriate choice of G reproduced empirical FC and dFC distributions. The optimal working point G^* depended systematically on the local regime: the *critical* model matched the data at low coupling ($G^* \approx 0.028$), the *supercritical* model required an intermediate coupling ($G^* \approx 0.070$), and the *subcritical* model achieved comparable fits only at higher coupling values ($G^* \approx 0.210$). This ordering is consistent with the higher sensitivity of critical neural masses, for which weaker interregional coupling suffices to coordinate large-scale dynamics [31]. Example simulated BOLD spatiotemporal heatmaps, FC matrices, and dFC matrices at each regime's working point [Fig. 3(c)] illustrate the corresponding qualitative differences in functional structure and variability. To assess whether the FC fit depends specifically on Allen-like structural connectivity, we additionally resimulated the critical regime on three structural-null surrogates of the Allen cortical connectome (a weight-shuffled full-density graph, a sparsified Allen backbone keeping only the strongest 15% of edges, and a sparse random graph with independent and identically distributed edges, matched in density and weight distribution (Figs. S5 and S6 in SM [28]). The empirical FC fit is reproduced only when Allen-like topology is preserved (full Allen and sparse Allen backbone) and is lost in both random-topology surrogates, indicating that the structural connectivity profile of the Allen connectome is necessary for empirical FC alignment.

D. Global criticality emerges at best fit of empirical data

We quantified how local tuning and long-range coupling shape global network signatures of criticality at the level of fast neuroelectric dynamics while initializing each region n in a common local regime [subcritical, critical, or supercritical; Fig. 4(a)]. At the optimal working point [i.e., the best fit to BOLD empirical data; Fig. 3(c)], all three configurations displayed the emergence of coordinated large-scale bursts, which can be visualized as quasi-instantaneous high-amplitude cofluctuations in the spatiotemporal $R_n(t)$ heatmaps in Fig. 4(b) [rows = region of interest (ROIs), columns = time, intensity = standardized population coherence $R_n(t)$; see Sec. IV C].

Starting from $G = 0$ and gradually increasing the global coupling, we inspected the effects of long-range connectivity on the corresponding global signal $\mathrm{GS}(t)$, defined as the average across all standardized ROI activities, $\mathrm{GS}(t) = \frac{1}{N}\sum_{n=1}^{N} z(R_n(t))$ [Fig. 4(c)]. Although stronger coupling promotes spatial coordination across regions in all three regimes, reflected in increased GS amplitude at higher G values, the temporal structure of $\mathrm{GS}(t)$ changed in regime-specific ways [Fig. 4(c)]: subcritical tuning produced progressively faster fluctuations; critical tuning amplified slow, aperiodic fluctuations over an intermediate G range; and supercritical tuning led to large-amplitude, quasioscillatory fast bursts at higher G.

To quantify these changes, we measured the AC1 of the global signal as a function of G (for the whole-brain signals, AC1 is computed at a 10-ms lag, which better resolves differences between couplings; see Sec. IV) [Fig. 4(d)]. In the subcritical regime (green), AC1 decreased monotonically with G, indicating that stronger recurrent coupling accelerated the relaxation of the population-average signal and thereby reduced its temporal persistence. In the critical regime (blue), AC1 displayed a pronounced, nonmonotonic dependence on G, peaking at intermediate coupling—an operating range in which interregional interactions optimally prolong global timescales. In the supercritical regime (red), AC1 decreased and displayed a minimum at intermediate G values, reflecting a nontrivial interaction between local oscillations and variability in their synchronization. As an independent corroboration, we computed DFA scaling exponent of $\mathrm{GS}(t)$ as a complementary indicator of long-range temporal correlations [32,33]: It also peaks at G^* with $H_{\mathrm{DFA}}(\mathrm{GS}) \approx 1$, at the canonical $1/f$-noise reference expected for critical dynamics (Fig. S7 of SM [28]). A natural concern, however, is that the AC1 rise at G^* might not reflect a genuine collective shift toward criticality but rather the passive smoothing of correlated long-range inputs by each region. To rule this out, we recorded the long-range input received by each region at G^* and replayed it into otherwise uncoupled neural masses: In this open-loop configuration, the global signal does not develop the AC1 peak (Fig. S8 in SM [28]), confirming that the signature requires the closed-loop dynamical coordination between regions enabled by the structural connectome.

We then probed global coordination through an avalanche analysis of $\mathrm{GS}(t)$ [Fig. 4(e)]. Global avalanches were defined as excursions of $\mathrm{GS}(t)$ above a threshold (the median of the time series). Each avalanche was characterized by its duration T, the number of 0.5-ms time steps of the excursion (avalanche sizes, i.e., excursion areas, give the same results; see Sec. IV). Power-law-like scaling in the distribution $P(T)$ emerged most prominently for critical local tuning at intermediate G, signaling the onset of scale-free, system-wide coordination. In contrast, subcritical networks produced steeper, truncated distributions (reflecting weak, rapidly damped excursions), whereas supercritical networks developed heavy tails at large S but with deviations from scale-free structure due to strongly driven, large-amplitude events.

Together, these findings indicate that global criticality is not achieved by coupling alone, but rather emerges from the interaction between local near-critical dynamics and intermediate coupling. Remarkably, signatures of global criticality obtained using the fast neuroelectric signals, such as the maximization of AC1(GS) [Fig. 4(d)] and of the power-law-like scaling range of global avalanches [Fig. 4(e)], emerged when local neural masses were tuned to criticality and the global coupling was set to the working point ($G = 0.028$) that best reproduced empirical mouse fMRI

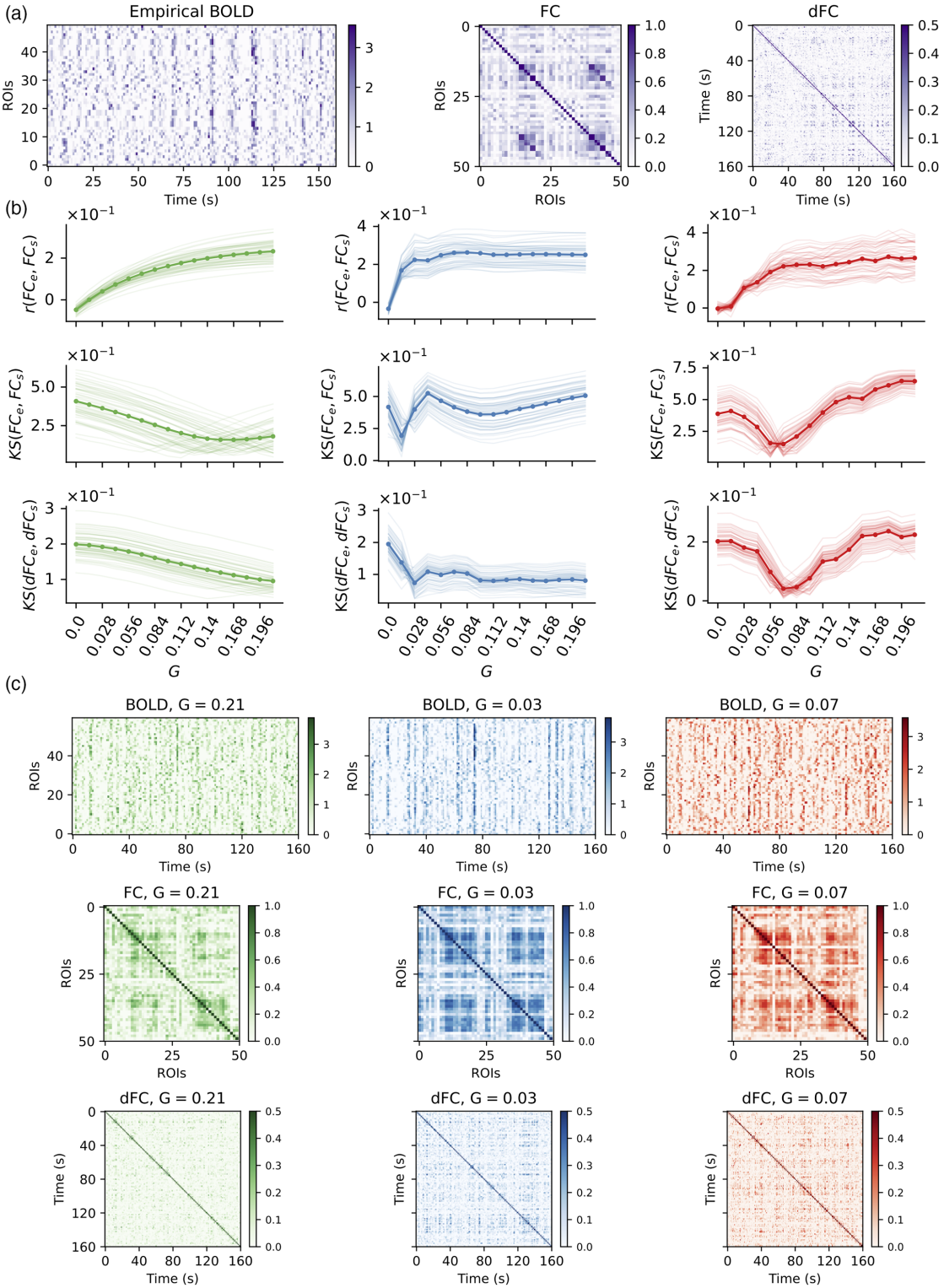


FIG. 3. Model performance against empirical fMRI data across dynamical regimes. (a) Empirical fMRI BOLD signal (left), FC (middle), and dFC (right) from an example mouse. (b) Comparison between simulated and empirical FC and dFC statistics across a range of global coupling values G, for subcritical (green), critical (blue), and supercritical (red) regimes. For each of these regimes, local parameters a and σ are fixed homogeneously across all ROIs as in Fig. 1(c). Each thin line represents one mouse. The thick line represents the average across mice. Top: correlation between simulated and empirical FC as a function of G. Middle: Kolmogorov-Smirnov (KS) distance between simulated and empirical FC distributions. Bottom: KS distance between simulated and empirical dFC distributions. In all metrics, the critical regime (blue) yields the best match to empirical data at intermediate G values. (c) Example simulated BOLD spatiotemporal heatmaps (top; rows = ROIs, columns = time, intensity = standardized BOLD signal), FC matrices (middle), and dFC matrices (bottom) at the optimal coupling G for each regime, illustrating qualitative differences in functional structure and variability.

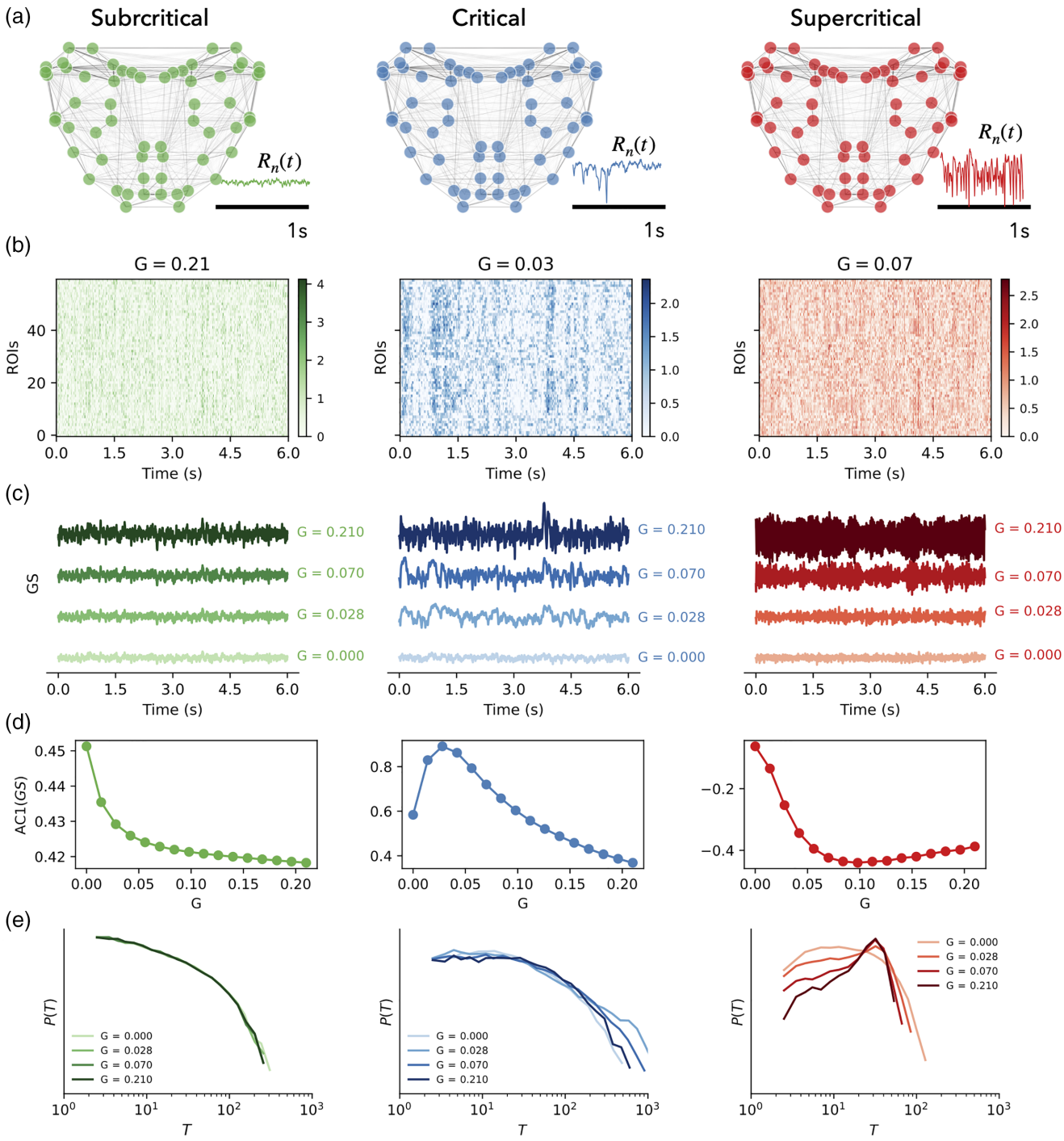


FIG. 4. Global signatures of criticality across whole-brain simulations. (a) Whole-cortex simulations of fast neuroelectric time series using the mouse structural connectome. All brain regions are initialized in either a subcritical (green), critical (blue), or supercritical (red) regime, and coupled via the anatomical connectivity. Example time series $R_n(t)$ illustrate the resulting local dynamics for each regime. (b) Spatiotemporal heatmaps of standardized $R_n(t)$ across all brain regions (rows = ROIs, columns = time, intensity = z-scored R_n) for three working point values of the global coupling strength G, under subcritical (green), critical (blue), and supercritical (red) local tuning. (c) Corresponding global signals, computed as the average across all standardized ROI activities. As G increases, the amplitude and temporal structure of the global signal change in regime-specific ways. (d) AC1 of the global signal GS(t) as a function of G. In the subcritical regime (green), AC1 decreases monotonically with G, indicating increasing desynchronization. In the critical regime (blue), AC1 peaks at intermediate G, revealing an optimal coupling range where global dynamics are closest to criticality. This optimal range coincides with the working point where simulations match the empirical data (Fig. 3). In the supercritical regime (red), AC1 is negative, decreases to a minimum at intermediate G ($G \approx 0.1$) and then increases slightly, consistent with dominance of strong local oscillations. (e) Distributions of global avalanche durations T, defined from threshold crossings of the global signal. The emergence of power-law-like scaling occurs most prominently in the critical case (blue) at intermediate G, indicating the onset of scale-free, globally coordinated dynamics.

data [thus, at the BOLD level; Figs. 3(b)–3(c)]. This alignment links global critical signatures to improved model-data correspondence.

E. Global criticality is reproduced in a whole-brain network of spiking neurons

In the whole-brain model, the regions interact through their mean-field phases [Eq. (6); see Sec. IV]. To test whether the global signatures above are a property of the underlying neuronal dynamics rather than of the reduced model, we simulated the full microscopic model of Eqs. (1) and (2): all 60 cortical regions, each a network of $K = 1000$ active rotators, coupled through the same Allen connectome (see Sec. IV). Each region was tuned to the hybrid-type transition of the *spiking* model, located by the maximum of the susceptibility of isolated populations, with AC1 peaking at the adjacent grid point (Fig. S13(a) in SM [28]) or just below it (subcritical). With regions at the transition, the global signal displayed a sharp peak at intermediate coupling in all three indicators: AC1 of the global signal increased from 0.966 ($G = 0$) to 0.991, its susceptibility increased 23-fold, and its DFA exponent rose from 0.67 to 1.04, the $1/f$ reference (Figs. S13(b)–S13(d) in SM [28]). The peak was confined to $0.021 < G < 0.035$ and was reproduced with an independent noise realization. At the same coupling, the correlation between regional susceptibility and in-strength changed sign (Figs. S13(b)–S13(d) in SM [28]), mirroring the sign-flipping in-strength gradient of the critical mean-field regime (Fig. S4(e) in SM [28]). With regions tuned just below the transition, all three indicators decreased monotonically with G, as in the subcritical mean-field regime. The spiking network therefore reproduces the central qualitative result of the mean-field model: Global criticality emerges at intermediate coupling only when the regions are tuned near their local transition. Still, the close agreement of the spiking peak location with the mean-field working point should not be overinterpreted, as the two models are not parametrized identically.

F. Long-range interactions produce heterogeneous shifts in criticality

Although regions are homogeneously initialized in a common local regime (subcritical, critical, or supercritical), long-range coupling drives the neural masses away from their initial state, consistent with our analysis in Fig. 2. We quantified how varying the coupling strength G modulates fast regional dynamics by measuring the AC1 of each simulated neuroelectric signal $R_n(t)$ at coupling G [Fig. 5(a)]. For each region n, we related the timescale $\mathrm{AC1}(R_n(t))$ emerging from large-scale coupling to its structural in-strength [i.e., the sum of incoming structural weights; Fig. 5(b)].

Across different starting regimes, coupling induces distinct, topology-dependent patterns: (1) Subcritical regime (green): For most regions, AC1 decreases monotonically with G, shifting dynamics away from criticality [Fig. 5(a)]. This decrease exhibits a pronounced topological gradient: Nodes with higher in-strength showed smaller AC1, consistent with faster timescales and stronger afferent drive accelerating local relaxation [Fig. 5(b)]. (2) Critical regime (blue): The highest AC1 is observed for weak G, bringing regions closer to criticality, but decreases at higher coupling G [Fig. 5(a)]. At the working point G^*, the relationship between AC1 and in-strength is strongly nonlinear: Regions with intermediate in-strength exhibit the fastest timescales, while both low- and high-in-strength regions retain slower timescales, yielding a U-shaped profile across the in-strength axis [Fig. 5(b)]. (3) Supercritical regime (red): Across coupling values, AC1 is predominantly negative, reflecting oscillatory dynamics rather than slow fluctuations [Fig. 5(a)]. Here, the relationship with in-strength is again monotonic; however, compared to the subcritical case, the timescales increase in magnitude, indicating stronger oscillatory persistence in regions with higher in-strength [Fig. 5(b)].

These regime-specific signatures are mirrored in the spectral statistics of exemplar regions [Fig. 5(c), top]. In the right retrosplenial area (a functional hub of the mouse connectome [34]), the power spectral density (PSD) reveals distinct spectral signatures across regimes. In the subcritical state, increasing global coupling flattens the $1/f$ slope. At criticality, when global coupling is tuned to the working point that best matches empirical data and yields global criticality ($G = 0.028$, Figs. 3 and 4), local activity exhibits a canonical $1/f$ decay. In the supercritical regime, coupling introduces additional high-frequency components, reflecting the emergence of new rhythms through long-range interactions. Consistently, local avalanche duration distributions in the retrosplenial area [Fig. 5(c), bottom] indicate that local criticality in whole-brain simulations emerges only within the critical regime (central panel) and only at the global coupling value corresponding to both global criticality and empirical fit ($G = 0.028$, Figs. 3 and 4).

A more comprehensive view of the interaction between coupling strength and node in-strength is provided in Fig. S4 SM [28], which shows the full two-dimensional phase diagram of $\mathrm{AC1}(R_n)$ over the (G, in-strength) plane for each regime [panels (a)–(c)], the Spearman rank correlation ρ between in-strength and AC1 as a function of G [panels (d)–(f)], and a high-in-strength contrast exemplar [VISal, panels (g)–(l)]. The in-strength–AC1 gradient is monotone negative across G in the sub- and supercritical regimes but is nonmonotonic and sign flipping in the critical regime (with the first sign reversal around G^*); a sign-flipping gradient is therefore a critical-regime-specific signature. The PSD and avalanche signatures of Fig. 5(c) carry over, and become more pronounced, at the cortical region of highest in-strength [VISal panels (g)–(l)].

Together, these findings demonstrate that the interplay between local criticality and global coupling shapes spatially structured gradients of timescales across the connectome, with AC1 modulation jointly determined by coupling strength and node in-strength, thereby enabling scale-free and flexible dynamics across scales.

III. DISCUSSION

In this work, we introduce a multiscale, connectome-based modeling framework that unites the study of local (between neurons in a brain region) and global (between regions across the entire brain) criticality within a single formalism. To our

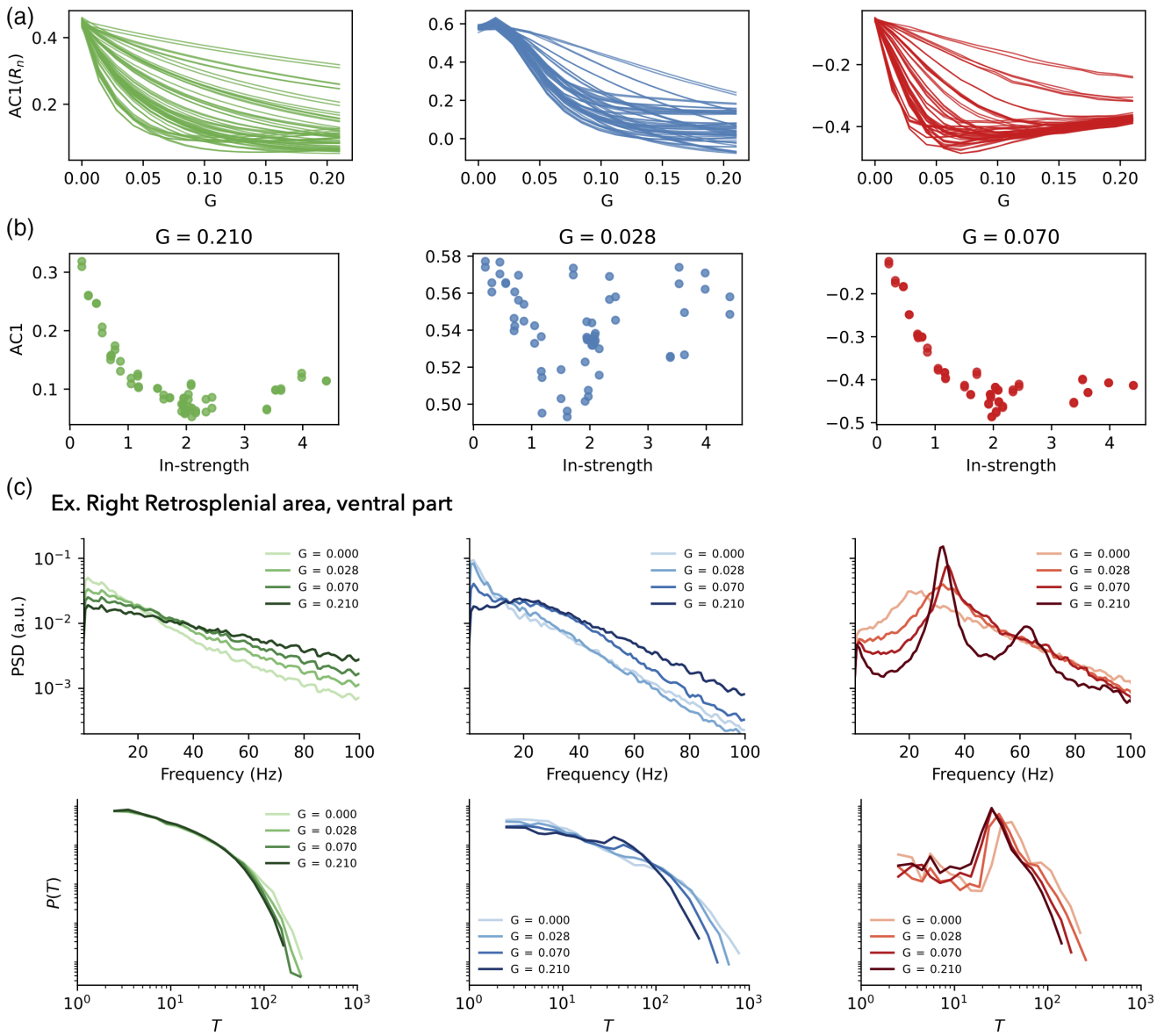


FIG. 5. Connectome-based simulations reveal interaction between local criticality and global coupling. (a) Effect of increasing the global coupling strength G on the AC1 of regional neuroelectric activity (one line per region). In the subcritical case (green), coupling monotonically decreases AC1, driving regions further from criticality. In the critical case (blue), AC1 initially increases with G, pushing regions closer to criticality before decreasing again. In the supercritical case (red), the effect of coupling is nonmonotonic and heterogeneous across regions. (b) AC1(R_n) at the working point G^* plotted against each region's in-strength (sum of incoming structural connectivity weights). In the subcritical and supercritical regimes, AC1 decreases with structural in-strength, reflecting a smooth gradient. In the critical regime, this relation is lost and nonlinear effects are more marked. (c) Example dynamics from the right retrosplenial area (ventral part). PSD shows characteristic spectral changes across regimes: $1/f$ steepening in the subcritical case, suppression of slow frequencies in the critical case, and emergence of fast oscillations in the supercritical case. Avalanche duration distributions for the same region further reveal that in the critical condition (blue), increased coupling slightly shifts dynamics toward a supercritical regime at higher G.

knowledge, this provides the first mechanistic model displaying the coemergence of near-critical dynamics at both the local and global scales, and offers a new avenue for investigating multiscale mechanisms of brain dynamics. By tuning the brain regions to subcritical, critical, and supercritical regimes, and embedding them in the empirically derived mouse connectome, we explored how local regimes interact through long-range anatomical connections to shape both regional and whole-brain dynamics. Our results demonstrate that the relationship between local and global criticality is neither trivial nor one directional: Global coupling provides an extrinsic modulation that shifts regional dynamics toward or away from criticality depending on their initial state [35], and conversely, the tuning of local regimes (here fixed as homogeneous) sets the conditions for the emergence/suppression of scale-free activity across the entire brain.

A key finding is that global signatures of criticality emerge most robustly when local populations are tuned near the

critical regime and coupled within an optimal range of global coupling. In this configuration, both empirical FC and dFC are best reproduced, and avalanche statistics display scale-free behavior at both the local and global levels. Based on the idea that criticality implies maximal sensitivity and susceptibility [9,31], this result suggests that the brain may benefit from enhanced functional properties in both neuronal communication and interactions between distributed areas. Thus, the local critical regime has the advantage of naturally reconciling local and global signatures of criticality within a single parameter setting. At the same time, we observed that subcritical and supercritical neural masses can also yield good correspondence with empirical FC, despite disrupting scale-free statistics. These regimes display distinctive features, such as emergent oscillations in the supercritical case (Fig. 5), that may be relevant for understanding diverse physiological and pathological states.

Comparison with structural-null surrogates of the Allen cortical connectome (Figs. S5 and S6 SM [28]) clarifies the role played by the Allen structure in our results. On one hand, it serves as a *generic* substrate: The emergence of coordinated dynamics at intermediate coupling [the AC1(GS) peak and the power-law-like global avalanche distribution at G^*] is preserved across any graph that matches Allen's weight distribution, regardless of topology or density. On the other hand, the Allen connectome imposes *specific* structural constraints that are not generic: Empirical mouse fMRI FC is reproduced only when the Allen-like strong-edge topology is preserved (full Allen, or the sparse Allen backbone keeping the top 15% of edges), and the suppression of high-G oversynchronization that prevents the network from locking requires both Allen-like topology and the long tail of weak edges.

A natural concern with our cross-scale validation is the timescale gap between the empirical BOLD fMRI data (sampled at TR $= 1$ s, with a hemodynamic filter interposed between neural activity and the observed signal) and the fast neural scale (2 kHz) at which the model's criticality claims live. We use BOLD because it is the only whole-brain empirical readout—covering subcortical as well as cortical regions—available for the anesthetized mouse, matching the full Allen-connectome coverage of our model; cortex-restricted optical methods, despite their higher temporal resolution, would not span the simulated network. The model is calibrated against this signal through a hemodynamic response function (see Sec. IV and Fig. S12 in [28]). The kernel acts as a low-pass operator that removes the fast-scale fingerprints of criticality (1/f spectrum, scale-free avalanches, fast AC1) from the BOLD signal while preserving the slow envelope of interregional coordination on the timescale of seconds. We therefore do not claim criticality at the BOLD level: The criticality claims in this article are stated at the fast electrophysiological scale, and BOLD enters only to constrain the model's operating point G^*. Across our four empirical-fit metrics (Fig. S11 in [28]), G^* is the smallest coupling at which all four reach their best-region values, and we adopt it as the operating point. Notably, this BOLD-derived G^* coincides with the coupling at which the fast neural-scale dynamics independently exhibit signatures of criticality: the sharp AC1(GS) peak corroborated by $H_{\mathrm{DFA}}(\mathrm{GS})$ at the canonical $1/f$ reference (Fig. S7 in SM [28]), the dependence on closed-loop coordination confirmed by the phase-randomized control (Fig. S8 in the SM [28]), and the regional $1/f$ spectra and scale-free avalanche distributions of Figs. 4 and 5. The convergence of BOLD-level and fast-scale signatures at the same operating point is therefore an emergent property of the model dynamics rather than a constraint built into the empirical-fit procedure.

At the regional level (Fig. 5), the effect of coupling is strongly modulated by structural in-strength, producing topological gradients of autocorrelation timescales that become nonlinear in the critical regime. These gradients link to the broader hypothesis that regions higher in the cortical hierarchy exhibit longer timescales [36,37] due to their proximity to criticality [30]. Anatomical constraints have been proposed as key determinants of such gradients [38–41]. Our results extend this view by showing that both local regime tuning and long-range coupling strength can shape the observed temporal hierarchy. In the brain *in vivo*, distance from criticality is typically estimated under conditions in which regions are already interconnected. Consequently, it remains unclear to what extent timescale gradients and fluctuations around criticality are shaped by intrinsic cytoarchitectural properties, neuromodulation, excitatory/inhibitory balance, versus long-range interactions [42].

These findings have important implications for understanding the fluctuations around criticality observed experimentally in local neuronal populations [43]. In particular, our results suggest that such fluctuations may not solely reflect local circuit properties or noise, but can also arise from top-down modulation via long-range interactions. This provides a mechanistic interpretation of recent electrophysiological observations that local criticality is not static but "fluid," varying across time and brain states [43]. In our framework, local populations near criticality can be transiently shifted toward sub- or supercritical dynamics by changes in input from connected regions (Fig. 2), which in turn are shaped by the evolving global state and the global coupling value. Alternatively, such fluctuations could be modeled via heterogeneous or time-varying local parameters. In general, different brain regions are characterized by distinct distances from criticality [30,44,45], and these distances may themselves be dynamically modulated across time, tasks, and brain states.

This perspective raises the possibility that the low-dimensional embedding of brain dynamics observed in many empirical datasets [46–48], where only a few principal components capture most of the variance, might reflect the imprint of large-scale network coordination on local dynamics. If fluctuations in local criticality are partly driven by global coupling, then the same long-range interactions that produce coherent low-dimensional trajectories could also regulate the temporal proximity of each region to its critical point.

Looking forward, our multiscale computational framework provides a platform for systematically investigating how structural connectivity, coupling strength, and heterogeneity in local tuning interact to produce the rich multiscale brain dynamics observed in experiments (see also Refs. [49–51]).

A minimal in-strength-aligned gradient of local parameters (Fig. S9 in SM [28]) recovers empirical FC but does not reproduce the AC1(GS) peak that defines global criticality in our framework, and is essentially indistinguishable from a

random-shuffle null on the headline metrics; a static structural gradient alone therefore does not seem sufficient to account for the regional variation in distance from criticality observed *in vivo* [30,43,44]. A more promising candidate is *dynamical* modulation of local parameters, plausibly under subcortical and neuromodulatory control [52,53], which in the companion paper [54] naturally reproduces the local fluctuations around criticality reported in cortex [43]; disentangling intrinsic, emergent, and dynamical contributions, and extending the analysis to subcortical regions, is left for future work.

As it stands, the model presents further limitations and could be extended in several other directions. For example, (1) exploring alternative structured patterns of local heterogeneity, e.g., gradients aligned with anatomical hierarchy or with neurotransmitter receptor maps, to identify configurations that may more flexibly produce both FC alignment and global-criticality signatures [55,56]; (2) incorporating time-varying parameters to simulate how task demands or neuromodulation may dynamically regulate the interaction between scales [52,53,57,58]; (3) exploring pathological alterations in either local or global regimes to predict how disruptions at one scale propagate to the other, providing mechanistic insights into disorders characterized by altered criticality (e.g., epilepsy [59], schizophrenia [60], Parkinson's disease [61], and brain lesions [62]); and (4) linking with low-dimensional manifold analyses to directly test whether the principal components of local criticality fluctuations align with large-scale network modes [46].

A methodological point concerns the coupling between regions. The mean-field reduction describes the local dynamics of each region, whereas the interregional interaction is modeled phenomenologically as a phase coupling between the regional collective oscillators (Sec. IV), the common choice for networks of neural oscillators. We validated this choice against simulations in which every region is a network of spiking neurons. At the spiking level, the key whole-brain result is reproduced: a peak of global AC1, susceptibility, and DFA exponent at intermediate coupling for regions tuned near their transition, and no peak for subcritical regions (Fig. S13 in SM [28]). The two-population effects of Fig. 2 are likewise reproduced (Fig. S14 in SM [28]). Two limitations remain. The spiking and mean-field models are compared qualitatively, relative to each model's own transition, because their parameter spaces do not map one-to-one (Fig. S2 in SM [28]). Furthermore, the spiking validation was performed at one network size ($K = 1000$ neurons per region).

An important next step is to further integrate the study of criticality across local and global scales, which have traditionally been investigated in relative isolation. Advances in large-scale electrophysiology now make it possible to record spiking activity from distributed neuronal populations across both inter- and intracortical circuits, offering an unprecedented opportunity to directly relate single-unit dynamics to systems-level critical fluctuations [63,64]. Such multiscale datasets will allow rigorous empirical tests of whether and how local signatures of criticality propagate to, constrain, or are modulated by global network interactions. In the accompanying study [54], we take a first step in this direction by analyzing simultaneous recordings of large neuronal populations across distant brain areas, providing an experimental counterpart to the theoretical framework developed here.

In conclusion, by embedding minimal models of local dynamics within the mouse connectome, we have shown that local and global criticality are dynamically intertwined, their relationship being shaped by both intrinsic tuning and the structure of long-range interactions. Such a unifying approach not only advances the theoretical understanding of brain criticality and its multiscale dynamics but also offers testable hypotheses for experiments capable of bridging microcircuit and systems-level observations.

IV. METHODS

A. Model rationale

We developed a multiscale connectome-based model to investigate local and global brain criticality within a unified framework. Building on the observation that isolated neuronal populations, such as those in organotypic cultures, exhibit spontaneous scale-free neuronal avalanches [7], we hypothesize that neuronal populations can display critical-like behavior when driven solely by noisy inputs in the absence of long-range connections, and that coupling such populations via the empirical structural connectome allows us to study the emergence of global coordination and its feedback on local regimes. The model was implemented in three steps [Fig. 1(a)]: (1) modeling the activity of an ROI as a network of neurons operating near criticality; (2) deriving a mean-field approximation that captures the critical-like dynamics while reducing computational complexity; and (3) simulating whole-brain activity by coupling ROIs through an empirical mouse connectome.

B. Neuron-level simulations

We modeled each ROI as a network of K interconnected neurons, represented as active rotators governed by the Shinomoto-Kuramoto model [23]:

$$\dot{\varphi}_{i,n}(t) = \omega + a\sin\varphi_{i,n}(t) + \frac{J}{K}\sum_{j=0}^{K}\sin[\varphi_{j,n}(t) - \varphi_{i,n}(t)] + \sigma\eta_{i,n}(t) + I_{i,n}(t), \quad (1)$$

where $\varphi_{i,n}$ is the phase of the ith neuron in ROI $n \in \{0,\ldots,M\}$, $\omega = 1$ is the intrinsic frequency, and $J = 1.25$ is the within-ROI all-to-all coupling strength. The population is driven by Gaussian white noise $\eta_{i,n}(t)$ of amplitude σ, and a is a local control parameter. Long-range coupling enters as an additive current:

$$I_{i,n}(t) = G\sum_{\substack{m\neq n\\ m=0}}^{M}\frac{W_{nm}}{K}\sum_{j\in m;j=0}^{K}\sin[\varphi_{j,m}(t-\tau_{nm}) - \varphi_{i,n}(t)], \quad (2)$$

where W_{nm} is the structural connection weight between ROIs n and m, τ_{nm} is the propagation delay, and G is the *global coupling* parameter.

For $G = 0$, Eq. (1) describes a disconnected ROI. This model exhibits an HT synchronization transition [24,25], where asynchronous states and incipient oscillations coexist, and where neuronal avalanche size and duration distributions span orders of magnitude [24]. For $G \neq 0$, local dynamics are

additionally shaped by long-range interactions according to the connectome.

C. Mean-field approximation

To reduce computational cost while retaining key dynamical properties, we adopted a mean-field description in terms of the Kuramoto order parameter:

$$R_n(t)e^{i\Psi_n(t)} = \langle e^{i\varphi_{i,n}(t)}\rangle_i. \tag{3}$$

For the decoupled case ($G = 0$), Ott-Antonsen theory [65] yields the following mean-field equations [24,25,66]:

$$\begin{aligned}\dot{R}_n(t) &= \frac{1}{2}R_n(t)\big[J\big(1-R_n^2(t)\big)-\sigma^2\big] \\ &\quad -\frac{1}{2}a\big(1-R_n^2(t)\big)\cos\Psi_n(t), \\ \dot{\Psi}_n(t) &= \omega + \frac{a\big(1+R_n^2(t)\big)\sin\Psi_n(t)}{2R_n(t)}.\end{aligned} \tag{4}$$

Relationship between $R_n(t)$ and underlying population activity. The complex Kuramoto order parameter $R_n(t)\,e^{i\Psi_n(t)}$ is the population average of the unit-modulus phase variables $e^{i\varphi_{i,n}(t)}$. Its modulus $R_n(t) \in [0, 1]$ measures the level of phase coherence in the population: $R_n \to 1$ when neurons within region n share a common phase (synchrony), $R_n \to 0$ when phases are uniformly distributed (asynchrony). Its argument $\Psi_n(t)$ is the population's average phase. In the active-rotator microscale model, an individual neuron emits a firing event when its phase wraps through 2π; the population firing rate is therefore proportional to the rate of wraparounds and, in synchronous regimes, tracks $R_n(t)$ closely (collective bursts of activity). Importantly, the mapping $R_n \leftrightarrow$ activity is regime dependent: In the supercritical and critical regimes, high R_n reflects high coordinated firing, whereas in the deeply subcritical regime, R_n can also be persistently high while firing is low, because phases are concentrated around a quiescent state (see Fig. S2 in SM [28] for the spiking-network counterpart). Throughout the article, $R_n(t)$ is reported directly. Spatiotemporal heatmaps in Figs. 3(c) and 4(b) show $R_n(t)z$ scored along time for each ROI; rows are ROIs, columns are time, and pixel intensity is the standardized value of R_n.

D. Identifying the bistable regime

We identified the bistable HT regime by scanning the (a, σ) parameter space of Eq. (4) (Fig. S1 in SM [28]). For each parameter pair, we performed 250 deterministic simulations with different initial conditions, computed the time averaged $R_n(t)$ for each run, and calculated the variance across initial conditions. This variance peaks in regions of bistability, where the final attractor depends on initial conditions. The resulting bistable region forms a triangular-shaped domain in (a, σ) space (Fig. S1 in SM [28]). Near the transition, the bistable window is narrow and the basin of one of the two attractors is small (at $\sigma = 0.677$, bistability is found for $0.9715 \leqslant a \leqslant 0.972$).

E. Whole-brain mean-field simulations

At the macroscale, brain regions are coupled through the empirical Allen tracer connectome (see Sec. IV G): Different region pairs have different weights W_{nm}, and the interregional structure is therefore weighted, directed, and anatomically constrained, in contrast to the within-region all-to-all coupling that enables the mean-field reduction. At the neuronal level [Eq. (2)], the coupling between any two connected regions is itself all-to-all: Every neuron of region m projects onto every neuron of region n with the same strength GW_{nm}/K, so that each neuron of region n receives the mean field of region m. This is what allows the interregional input to be written in terms of the regional order parameters [Eq. (6)]. The whole-brain model consists of $2M$ stochastic differential equations:

$$\begin{aligned}\dot{R}_n(t) &= \frac{1}{2}R_n(t)\big[J\big(1-R_n^2(t)\big)-\sigma^2\big] \\ &\quad -\frac{1}{2}a\big(1-R_n^2(t)\big)\cos\Psi_n(t), \\ \dot{\Psi}_n(t) &= \omega + \frac{a\big(1+R_n^2(t)\big)\sin\Psi_n(t)}{2R_n(t)} + \delta_{\psi,n}(t) + I_n^{\mathrm{MF}}(t),\end{aligned} \tag{5}$$

where we introduced a weak Gaussian noise term $\delta_{\psi,n}(t)$ with standard deviation $N = 0.0001$ to $\dot{\Psi}_n(t)$ in Eq. (4) to emulate realistic fluctuations and recover avalanchelike dynamics in the bistable HT regime. The mean-field network input is

$$I_n^{\mathrm{MF}}(t) = G\sum_{\substack{m\neq n\\ m=0}}^{M} W_{nm}R_m(t-\tau_{nm})\sin\left[\Psi_m(t-\tau_{nm})-\Psi_n(t)\right], \tag{6}$$

where W_{nm} are the weights of the structural connectome and we employed null delays $\tau_{nm} = 0$ for simplicity.

The interregional input of Eq. (6) acts on the regional phases Ψ_n, the standard form of coupling in Kuramoto-type networks of neural oscillators. This phenomenological coupling is a modeling choice. It corresponds to the Ott-Antonsen reduction of the interregional current of Eq. (2) in the limit of highly coherent regions ($R_n \to 1$), in which the input acts on the regional phases only; at our operating points ($R_n \approx$ 0.7–0.8), the prefactor of the phase term in that reduction, $(1 + R_n^2)/(2R_n)$, is within 5% of one. We validated this coupling against simulations of the full microscopic model in which every region is a network of spiking neurons (next subsection; Figs. S13 and S14 in SM [28]).

F. Spiking-network validation

Whole-brain spiking network. To validate the mean-field results at the neuronal level, we simulated the microscopic model of Eqs. (1) and (2) for all $M = 60$ cortical regions, each a population of $K = 1000$ active rotators, coupled through the Allen connectome with null delays; as in Eq. (2), the coupling between any two connected regions is all-to-all at the neuronal level, with strength GW_{nm}/K. Because the mean-field and spiking parameter spaces do not map one-to-one (Fig. S2 in SM [28]), the spiking regions were tuned relative to the hybrid-type transition of the spiking model, using the parameters of Fig. S2 in SM [28] and Ref. [24] ($J = 1$, $\sigma = 0.499$, $\omega = 1$). The transition was located by simulating isolated populations of the same size ($K = 1000$, $G = 0$, 60 s) on a grid $a \in [1.05, 1.09]$ (step 0.0025). The susceptibility (below) of $R(t)$ peaks at

$a_c = 1.070$ and AC1 at the adjacent grid point ($a = 1.0725$), just before the discontinuous jump of R to the quiescent state; we set the critical regime at a_c (Fig. S13(a) in SM [28]). Whole-brain simulations were run with all regions at $a = a_c$ (critical) or at $a = a_c + 0.005$ (subcritical), for $G \in \{0, 0.014, 0.021, 0.028, 0.035, 0.042, 0.056, 0.084, 0.112, 0.168\}$ (critical) and $G \in \{0, 0.014, 0.028, 0.042, 0.056, 0.084, 0.112, 0.168\}$ (subcritical), 120 s each, with a second noise realization at the peak coupling. The interregional sum of Eq. (2) was evaluated exactly through the presynaptic order parameters, $\frac{1}{K}\sum_{j\in m}\sin(\varphi_{j,m} - \varphi_{i,n}) = R_m \sin(\Psi_m - \varphi_{i,n})$, which reduces the cost per step from $O(MK^2)$ to $O(MK)$ without approximation. Equations were integrated with a stochastic Heun scheme ($dt = 0.05$ ms, independent Gaussian noise of amplitude $\sigma\sqrt{dt}$ per neuron), and $R_n(t)$ was stored at 2 kHz after discarding the first 2.5 s. The global signal was the population average of $R_n(t)$ over the 60 regions.

Two coupled spiking populations. For the spiking counterpart of Fig. 2 (Fig. S14 in SM [28]), two populations of $K = 5000$ active rotators ($J = 1$, $\sigma = 0.499$) were coupled all-to-all (every neuron of the source population projecting onto every neuron of the target with strength G/K, i.e., $W = 1$) with $G = 0.05$, either feedforward (A $\rightarrow$ B) or mutually (A $\leftrightarrow$ B). Here, the transition of isolated $K = 5000$ populations was located at $a_c = 1.070$ (scan of $a \in [0.97, 1.08]$, step 0.0025), and (a_A, a_B) were varied on a 7×7 grid $a_c + 0.01\,k$, $k = -3, \ldots, 3$, spanning the supercritical ($a < a_c$), critical and subcritical ($a > a_c$) sides of the spiking transition. Each condition was simulated for 60 s together with isolated references at each a; all systems of a condition were integrated in parallel as a single network with block-diagonal connectivity. The change of the target's AC1 was quantified exactly as in Figs. 2(g) and 2(h), and complemented by the change of its susceptibility.

G. Allen mouse structural connectome

The structural connectivity matrix W_{nm} used in our simulations was derived from the tracer-based Allen Mouse Brain Connectivity Atlas [26], processed through the Virtual Mouse Brain pipeline [27], and previously employed in related work [62]. In these experiments, adult male C57Bl/6J mice received localized injections of a recombinant adeno-associated virus expressing an anterograde enhanced green fluorescent protein tracer. Tracer migration was imaged using serial two-photon tomography, revealing axonal projections from the injection site across the brain.

Injection density in each source region was defined as the fraction of infected pixels relative to the total number of pixels in that region. Projection density in a target region was quantified as the number of pixels carrying tracer signal, normalized by the total pixel count in that target. The directed connection strength from region n (source) to region m (target) was then computed as the ratio between projection density at m and injection density at n.

To construct the full connectome, we averaged the tracer data across injection experiments performed in the right hemisphere and considered projections to both ipsilateral and contralateral targets. This procedure yielded a weighted, directed connectivity matrix spanning 148 anatomical ROIs, including cortical and subcortical areas. For the present study, we restricted the analysis to the 60 cortical ROIs corresponding to our simulation parcellation (Fig. S3 in SM [28]). The final connectivity matrix was normalized such that all weights lie between 0 and 1. At the cortical 60-region level, the Allen connectome is densely populated, with ∼99% of off-diagonal entries nonzero and a heavy-tailed weight distribution, consistent with the ultradense interareal mouse cortical connectome reported from recent tracer-based reconstructions [67]. Three structural-null surrogates of this connectome are used for the analyses of Figs. S5 and S6 in SM [28]; their construction is described in the caption of Fig. S5 in SM [28].

H. Empirical dataset

The data used in this study are part of a unified mouse resting-state functional MRI (rs-fMRI) resource collected by Dr. Joanes Grandjean and collaborators across two laboratories: ETH Zurich and the Singapore Bioimaging Consortium [68]. All data were obtained from the publicly available repository [68]. The datasets were preprocessed using a standardized pipeline to ensure comparability and consistency across experimental conditions.

To focus on a homogeneous control population, we included animals only if they were wild type in genotype, classified as controls, scanned under the standardized medetomidine-isoflurane (mediso) protocol, and passed the quality assurance diagnostic tests ("pass"). This yielded a final sample of 53 wild-type control animals (dataset label *CPS_ctl* within the chronic social defeat, CSD1, collection).

Data acquisition was performed at a field strength of 9.4 T using a cryogenically cooled phased-array receiver coil. rs-fMRI scans were acquired with TR = 1 s, TE = 9.2 ms, and consisted of 360 volumes per run, corresponding to a total acquisition time of 6 min. The mediso anesthesia protocol (medetomidine for sedation and low-dose isoflurane for maintenance) was used, as it minimizes physiological stress while preserving resting-state network activity.

The preprocessed time series were aligned to the Allen Institute for Brain Science (AIBS) reference atlas, resampled to a resolution of 0.2 mm × 0.2 mm × 0.2 mm (voxel volume 0.008 mm^3). Out of the 604 regions defined in the AIBS atlas, we selected a subset of 60 cortical ROIs, corresponding to the parcellation used in our brain simulations (Fig. S3 in SM [28]). Posterior cortical regions prone to imaging artifacts were excluded.

The resulting dataset therefore consisted of preprocessed rs-fMRI time series from 60 cortical ROIs across 53 animals, which served as the empirical benchmark for functional connectivity and dynamic analyses in comparison with simulated data (see Sec. IV I).

I. Comparison with empirical data

Whole-brain model results correspond to simulated neuroelectric signals $R_n(t)$ at 2000 Hz time resolution for each brain region n, which were used for local and global criticality analyses. To compare our simulations to empirical data, these fast signals were convolved with a Balloon-Windkessel

hemodynamic response function and z scored, resulting in simulated BOLD (standardized) signals $B_n(t)$ at TR = 1 s. FC was computed as Pearson correlations between ROIs, and dFC from correlations between edge coactivation patterns $E_{nm}(t) = B_n(t) \times B_m(t)$ at different times t_i and t_j [69,70]. For each G, we computed FC correlations and Kolmogorov-Smirnov distances between simulated and empirical FC/dFC distributions to identify the optimal $G^\star$ range. The hemodynamic response function is the first-order Volterra form of the Balloon-Windkessel kernel [71], implemented in the `Bold` monitor of The Virtual Brain (TVB) simulator at its default parameter values (see Fig. S12 in SM [28] for the kernel shape). Convolution with this kernel followed by sampling at TR = 1 s acts as a low-pass operator that attenuates fast neural fluctuations while preserving the slow envelope of population coordination, which is the timescale on which BOLD FC is computed.

J. Criticality indicators

We complement the main-text AC1 with two further analyses on the global signal GS(t): The DFA scaling exponent H_{DFA} [32], as an independent indicator of long-range temporal correlations (Fig. S7 in SM [28]), and a phase-randomized afferent control that probes whether the AC1(GS) peak at G^* reflects closed-loop dynamical coordination or passive integration of correlated inputs (Fig. S8 in the SM [28]).

Autocorrelation (AC1). AC1 is the autocorrelation of a signal at a lag of 20 samples. For the single-region and two-population mean-field simulations (Figs. 1 and 2), analyzed at the 20 kHz integration rate, this corresponds to 1 ms. For the whole-brain mean-field signals, stored at 2 kHz (Figs. 4 and 5 and related Supplemental figures), it corresponds to 10 ms. At a 1-ms lag, AC1 of the whole-brain signals is close to one for all couplings (0.97–0.998 for the global signal), which compresses the differences between conditions; the 10-ms lag resolves them. The global-signal AC1 peak at G^* in the critical regime, and its absence in the subcritical regime, are unchanged when AC1 is evaluated at 1 ms; the rereversal of the in-strength gradient at large G (Fig. S4(e) in SM [28]) is specific to the 10-ms lag. For the spiking-network validation (Figs. S13 and S14 in SM [28]), AC1 is evaluated at 1 ms (lag of 2 samples at 2 kHz), since a fixed-lag autocorrelation does not depend on the sampling rate.

Susceptibility (χ). As a complementary indicator of proximity to a transition, used for the spiking-network validation, we computed the susceptibility of the order parameter, $\chi = \mathrm{Var}[\tilde{R}(t)]$, where $\tilde{R}$ is the regional $R_n(t)$ or the global population-averaged $R(t)$ after low-pass filtering with a zero-phase fourth-order Butterworth filter at 5 Hz (200-ms timescale). The filter removes fast collective oscillations, which would otherwise dominate the variance on the oscillatory side of the transition, and retains the slow fluctuations that grow near the transition.

Avalanche durations and sizes. Avalanches are defined as excursions of a signal beyond its median (above the median for the global signal, below it for regional signals; Figs. 1–5). For each excursion, we measure its duration T (number of time steps) and its size S (area between the signal and the threshold). Figure 1(d) shows both; the other avalanche panels (Figs. 2, 4(e), 5(c), and Figs. S4, S6, and S9 in SM [28]) show duration distributions $P(T)$. Sizes and durations are tightly related: in the critical regime of the isolated population $S \propto T^{2.0}$ [Fig. 1(d)], and for the global-signal avalanches the Spearman correlation between S and T is 0.95–0.99 across regimes and couplings. For Fig. 1(d), exponents were estimated by maximum likelihood (`powerlaw` package, lower cutoff at the median) for sizes ($\tau = 1.42$) and durations ($\alpha = 1.80$), with $\gamma = 2.00$ from a log-log fit of S versus T; the crackling-noise prediction $(\alpha - 1)/(\tau - 1) = 1.89$ agrees with γ within 6%, and a log-likelihood-ratio test favors a power law over an exponential distribution in the critical regime ($p < 10^{-13}$) but not in the sub- or supercritical regimes. The size distributions $P(S)$ therefore lead to the same conclusions: for instance, the broadest, most power-law-like distributions are found for critical tuning at G^* for both $P(T)$ and $P(S)$ (largest global avalanche: $T = 1478$ steps and $S = 985$, versus $T = 426$ and $S = 71$ at $G = 0$).

DFA scaling exponent (H_{DFA}). We apply detrended fluctuation analysis to GS(t) and to each $R_n(t)$ following [32], with polynomial detrending of order 1 and log-spaced window sizes between 16 ms and 8 s, using the `nolds` Python package. The fluctuation function scales as $F(w) \sim w^{H_{\mathrm{DFA}}}$; reference values are $H_{\mathrm{DFA}} = 0.5$ for white noise, ≈ 1 for $1/f$ noise, and 1.5 for integrated white noise, with critical-regime long-range correlations expected to give $H_{\mathrm{DFA}} \approx 1$ (Fig. S7 in SM [28]).

Phase-randomized afferent control. We recorded the interregional input $I_n^{\mathrm{MF}}(t)$ received by each region in the critical-regime Allen simulation at G^*, built a Fourier phase-randomized surrogate that preserves the input's exact power spectrum but destroys its causal temporal structure, and replayed both the recorded and the phase-randomized inputs through the *uncoupled* mean-field model. Each open-loop condition was run for $n = 25$ independent replicates varying initial conditions, integration noise seed, and (for the phase-randomized case) the surrogate-input seed. In both open-loop configurations, the AC1(GS) value collapses well below the coupled value, indicating that the global signature at G^* requires the closed-loop dynamical coordination between regions enabled by the structural connectome (Fig. S8 in SM [28]).

ACKNOWLEDGMENTS

G.R. acknowledges support from the Marie Skłódowska-Curie Postdoctoral Fellowship (Project CAERUS) under the European Union's Horizon Europe research and innovation programme (Grant No. 101199894). L.D.P. acknowledges support from the Brazilian agency CNPq (Grant No. 444500/2024-3). Data were provided (in part) by the Donders Institute for Brain, Cognition and Behaviour, Radboud University Nijmegen.

G.R. and L.D.P. designed research; G.R., P.B., D.D., and B.N. performed simulations; G.R. preprocessed experimental data; G.R., P.B., and L.D.P. analyzed data; G.R. and L.D.P. organized results; G.R. wrote the first draft; all authors discussed the results and wrote the paper.

DATA AVAILABILITY

The data that support the findings of this article are openly available. The empirical resting-state fMRI data are part of the mouse rs-fMRI resource of Grandjean and collaborators, available in Ref. [68] under a CC-BY 4.0 license. The structural connectome is derived from the Allen Mouse Brain Connectivity Atlas. All code to reproduce the simulations and analyses is available in Ref. [72].

[1] J. M. Beggs, The criticality hypothesis: How local cortical networks might optimize information processing, Philos. Trans. R. Soc. A **366**, 329 (2008).

[2] L. Cocchi, L. L. Gollo, A. Zalesky, and M. Breakspear, Criticality in the brain: A synthesis of neurobiology, models and cognition, Prog. Neurobiol. **158**, 132 (2017).

[3] V. Zimmern, Why brain criticality is clinically relevant: A scoping review, Front. Neural Circuits **14**, 54 (2020).

[4] J. O'Byrne and K. Jerbi, How critical is brain criticality? Trends Neurosci. **45**, 820 (2022).

[5] K. B. Hengen and W. L. Shew, Is criticality a unified setpoint of brain function? Neuron **113**, 2582 (2025).

[6] K. Linkenkaer-Hansen, V. V. Nikouline, J. M. Palva, and R. J. Ilmoniemi, Long-range temporal correlations and scaling behavior in human brain oscillations, J. Neurosci. **21**, 1370 (2001).

[7] J. M. Beggs and D. Plenz, Neuronal avalanches in neocortical circuits, J. Neurosci. **23**, 11167 (2003).

[8] W. L. Shew, H. Yang, S. Yu, R. Roy, and D. Plenz, Information capacity and transmission are maximized in balanced cortical networks with neuronal avalanches, J. Neurosci. **31**, 55 (2011).

[9] W. L. Shew and D. Plenz, The functional benefits of criticality in the cortex, Neuroscientist **19**, 88 (2013).

[10] E. Tognoli and J. A. Kelso, The metastable brain, Neuron **81**, 35 (2014).

[11] J. M. Beggs and D. Plenz, Neuronal avalanches are diverse and precise activity patterns that are stable for many hours in cortical slice cultures, J. Neurosci. **24**, 5216 (2004).

[12] J. M. Palva, A. Zhigalov, J. Hirvonen, O. Korhonen, K. Linkenkaer-Hansen, and S. Palva, Neuronal long-range temporal correlations and avalanche dynamics are correlated with behavioral scaling laws, Proc. Natl. Acad. Sci. USA **110**, 3585 (2013).

[13] G. M. Duma, A. Danieli, G. Mento, V. Vitale, R. S. Opipari, V. Jirsa, P. Bonanni, and P. Sorrentino, Altered spreading of neuronal avalanches in temporal lobe epilepsy relates to cognitive performance: A resting-state hdEEG study, Epilepsia **64**, 1278 (2023).

[14] O. Shriki, J. Alstott, F. Carver, T. Holroyd, R. N. Henson, M. L. Smith, R. Coppola, E. Bullmore, and D. Plenz, Neuronal avalanches in the resting MEG of the human brain, J. Neurosci. **33**, 7079 (2013).

[15] V. Priesemann, M. Valderrama, M. Wibral, M. Le Van Quyen, and O. Sporns, Neuronal avalanches differ from wakefulness to deep sleep—Evidence from intracranial depth recordings in humans, PLoS Comput. Biol. **9**, e1002985 (2013).

[16] A. Zhigalov, G. Arnulfo, L. Nobili, S. Palva, and J. M. Palva, Relationship of fast- and slow-timescale neuronal dynamics in human MEG and SEEG, J. Neurosci. **35**, 5385 (2015).

[17] E. Tagliazucchi, P. Balenzuela, D. Fraiman, and D. R. Chialvo, Criticality in large-scale brain fMRI dynamics unveiled by a novel point process analysis, Front. Physiol. **3**, 15 (2012).

[18] M. Yaghoubi, T. de Graaf, J. G. Orlandi, F. Girotto, M. A. Colicos, and J. Davidsen, Neuronal avalanche dynamics indicates different universality classes in neuronal cultures, Sci. Rep. **8**, 3417 (2018).

[19] Z. Bowen, D. E. Winkowski, S. Seshadri, D. Plenz, and P. O. Kanold, Neuronal avalanches in input and associative layers of auditory cortex, Front. Syst. Neurosci. **13**, 45 (2019).

[20] G. F. Grosu, A. V. Hopp, V. V. Moca, H. Bârzan, A. Ciuparu, M. Ercsey-Ravasz, M. Winkel, H. Linde, and R. C. Mureşan, The fractal brain: Scale-invariance in structure and dynamics, Cereb. Cortex **33**, 4574 (2023).

[21] M. Cirunay, G. Ódor, I. Papp, and G. Deco, Scale-free behavior of weight distributions of connectomes, Phys. Rev. Res. **7**, 013134 (2025).

[22] M. Axer and K. Amunts, Scale matters: The nested human connectome, Science **378**, 500 (2022).

[23] S. Shinomoto and Y. Kuramoto, Phase transitions in active rotator systems, Prog. Theor. Phys. **75**, 1105 (1986).

[24] V. Buendía, P. Villegas, R. Burioni, and M. A. Muñoz, Hybrid-type synchronization transitions: Where incipient oscillations, scale-free avalanches, and bistability live together, Phys. Rev. Res. **3**, 023224 (2021).

[25] V. Klinshov and I. Franović, Two scenarios for the onset and suppression of collective oscillations in heterogeneous populations of active rotators, Phys. Rev. E **100**, 062211 (2019).

[26] S. W. Oh, J. A. Harris, L. Ng, B. Winslow, N. Cain, S. Mihalas, Q. Wang, C. Lau, L. Kuan, A. M. Henry, *et al.*, A mesoscale connectome of the mouse brain, Nature (London) **508**, 207 (2014).

[27] F. Melozzi, M. M. Woodman, V. K. Jirsa, and C. Bernard, The virtual mouse brain: A computational neuroinformatics platform to study whole mouse brain dynamics, eNeuro **4**, ENEURO.0111-17.2017 (2017).

[28] See Supplemental Material at http://link.aps.org/supplemental/10.1103/n87d-5krk for Supplemental Material Figs. S1–S14: local dynamical regimes and bistability of the mean-field model, single-neuron simulations, the Allen connectome and regional in-strength, structural-null surrogate connectomes, AC1 and DFA analyses, the phase-randomized afferent control, structured heterogeneity of local criticality, cross-scale alignment of BOLD and neural criticality signatures, the hemodynamic response function, and validation with networks of spiking neurons.

[29] M. Scheffer, J. Bascompte, W. A. Brock, V. Brovkin, S. R. Carpenter, V. Dakos, H. Held, E. H. van Nes, M. Rietkerk, and G. Sugihara, Early-warning signals for critical transitions, Nature (London) **461**, 53 (2009).

[30] B. Harris, L. L. Gollo, and B. D. Fulcher, Tracking the distance to criticality in systems with unknown noise, Phys. Rev. X **14**, 031021 (2024).

[31] O. Kinouchi and M. Copelli, Optimal dynamical range of excitable networks at criticality, Nat. Phys. **2**, 348 (2006).

[32] C.-K. Peng, S. V. Buldyrev, S. Havlin, M. Simons, H. E. Stanley, and A. L. Goldberger, Mosaic organization of DNA nucleotides, Phys. Rev. E **49**, 1685 (1994).

[33] R. Hardstone, S.-S. Poil, G. Schiavone, R. Jansen, V. V. Nikulin, H. D. Mansvelder, and K. Linkenkaer-Hansen, Detrended fluctuation analysis: A scale-free view on neuronal oscillations, Front. Physiol. **3**, 450 (2012).

[34] A. Liska, A. Galbusera, A. J. Schwarz, and A. Gozzi, Functional connectivity hubs of the mouse brain, NeuroImage **115**, 281 (2015).

[35] B. Mariani, G. Nicoletti, M. Bisio, M. Maschietto, S. Vassanelli, and S. Suweis, Disentangling the critical signatures of neural activity, Sci. Rep. **12**, 10770 (2022).

[36] J. D. Murray, A. Bernacchia, D. J. Freedman, R. Romo, J. D. Wallis, X. Cai, C. Padoa-Schioppa, T. Pasternak, H. Seo, D. Lee, *et al.*, A hierarchy of intrinsic timescales across primate cortex, Nat. Neurosci. **17**, 1661 (2014).

[37] A. Ponce-Alvarez, Network mechanisms underlying the regional diversity of variance and time scales of the brain's spontaneous activity fluctuations, J. Neurosci. **45**, e1699242024 (2025).

[38] S. J. Kiebel, J. Daunizeau, and K. J. Friston, A hierarchy of time-scales and the brain, PLoS Comput. Biol. **4**, e1000209 (2008).

[39] R. Chaudhuri, K. Knoblauch, M.-A. Gariel, H. Kennedy, and X.-J. Wang, A large-scale circuit mechanism for hierarchical dynamical processing in the primate cortex, Neuron **88**, 419 (2015).

[40] R. V. Raut, A. Z. Snyder, and M. E. Raichle, Hierarchical dynamics as a macroscopic organizing principle of the human brain, Proc. Natl. Acad. Sci. USA **117**, 20890 (2020).

[41] J. Liang, Z. Yang, and C. Zhou, Excitation–inhibition balance, neural criticality, and activities in neuronal circuits, Neuroscientist **31**, 31 (2025).

[42] E. J. Müller, B. R. Munn, and J. M. Shine, The brain that controls itself, Curr. Opin. Behav. Sci. **63**, 101499 (2025).

[43] A. J. Fontenele, N. A. P. de Vasconcelos, T. Feliciano, L. A. A. Aguiar, C. Soares-Cunha, B. Coimbra, L. Dalla Porta, S. Ribeiro, A. J. Rodrigues, N. Sousa, *et al.*, Criticality between cortical states, Phys. Rev. Lett. **122**, 208101 (2019).

[44] G. B. Morales, S. di Santo, and M. A. Muñoz, Quasiuniversal scaling in mouse-brain neuronal activity stems from edge-of-instability critical dynamics, Proc. Natl. Acad. Sci. USA **120**, e2208998120 (2023).

[45] G. G. Cambrainha, D. M. Castro, L. L. Gollo, P. V. Carelli, and M. Copelli, Hierarchical organization of critical brain dynamics, arXiv:2604.21832.

[46] A. J. Fontenele, J. S. Sooter, V. K. Norman, S. H. Gautam, and W. L. Shew, Low-dimensional criticality embedded in high-dimensional awake brain dynamics, Sci. Adv. **10**, eadj9303 (2024).

[47] A. E. Cathignol, L. Kusch, M. Angiolelli, E. T. Lopez, A. Polverino, A. Romano, G. Sorrentino, V. Jirsa, G. Rabuffo, and P. Sorrentino, Magnetoencephalography dimensionality reduction informed by dynamic brain states, Eur. J. Neurosci. **61**, e70128 (2025).

[48] M. G. Perich, D. Narain, and J. A. Gallego, A neural manifold view of the brain, Nat. Neurosci. **28**, 1582 (2025).

[49] S.-J. Wang, C. C. Hilgetag, and C. Zhou, Sustained activity in hierarchical modular neural networks: Self-organized criticality and oscillations, Front. Comput. Neurosci. **5**, 30 (2011).

[50] R. Russo, H. J. Herrmann, and L. de Arcangelis, Brain modularity controls the critical behavior of spontaneous activity, Sci. Rep. **4**, 4312 (2014).

[51] S. Okujeni and U. Egert, Structural modularity tunes mesoscale criticality in biological neuronal networks, J. Neurosci. **43**, 2515 (2023).

[52] B. R. Munn, E. J. Müller, G. Wainstein, and J. M. Shine, The ascending arousal system shapes neural dynamics to mediate awareness of cognitive states, Nat. Commun. **12**, 6016 (2021).

[53] R. Gao, R. L. Van den Brink, T. Pfeffer, and B. Voytek, Neuronal timescales are functionally dynamic and shaped by cortical microarchitecture, eLife **9**, e61277 (2020).

[54] L. Dalla Porta, P. Bozzo, M. N. Pompili, D. Depannemaecker, A. J. Fontenele, T. Fukai, P. Sorrentino, and G. Rabuffo, companion paper, Intra- and interhemispheric signatures of criticality at the onset of synchronization, PRX Life **4**, 043014 (2026).

[55] G. Deco, M. L. Kringelbach, A. Arnatkeviciute, S. Oldham, K. Sabaroedin, N. C. Rogasch, K. M. Aquino, and A. Fornito, Dynamical consequences of regional heterogeneity in the brain's transcriptional landscape, Sci. Adv. **7**, eabf4752 (2021).

[56] L. Dalla Porta, J. Fousek, A. Destexhe, and M. V. Sanchez-Vives, Spatially structured heterogeneity shapes large-scale cortical dynamics in a model of the human cortex, Proc. Natl. Acad. Sci. USA **123**, e2532072123 (2026).

[57] M. Nazari, J. Karimi Abadchi, M. Naghizadeh, E. J. Bermudez-Contreras, B. L. McNaughton, M. Tatsuno, and M. H. Mohajerani, Regional variation in cholinergic terminal activity determines the non-uniform occurrence of cortical slow waves during REM sleep in mice, Cell Rep. **42**, 112450 (2023).

[58] R. Zeraati, Y.-L. Shi, N. A. Steinmetz, M. A. Gieselmann, A. Thiele, T. Moore, A. Levina, and T. A. Engel, Intrinsic timescales in the visual cortex change with selective attention and reflect spatial connectivity, Nat. Commun. **14**, 1858 (2023).

[59] S. Liu, F. Li, and F. Wan, Distance to criticality undergoes critical transition before epileptic seizure attacks, Brain Res. Bull. **200**, 110684 (2023).

[60] G. Alamian, T. Lajnef, A. Pascarella, J.-M. Lina, L. Knight, J. Walters, K. D. Singh, and K. Jerbi, Altered brain criticality in schizophrenia: New insights from magnetoencephalography, Front. Neural Circuits **16**, 630621 (2022).

[61] P. Sorrentino, R. Rucco, F. Baselice, R. De Micco, A. Tessitore, A. Hillebrand, L. Mandolesi, M. Breakspear, L. L. Gollo, and G. Sorrentino, Flexible brain dynamics underpins complex behaviours as observed in Parkinson's disease, Sci. Rep. **11**, 4051 (2021).

[62] G. Rabuffo, H.-A. Lokossou, Z. Li, A. Ziaee-Mehr, M. Hashemi, P. P. Quilichini, A. Ghestem, O. Arab, M. Esclapez, P. Verma, *et al.*, Mapping global brain reconfigurations following local targeted manipulations, Proc. Natl. Acad. Sci. USA **122**, e2405706122 (2025).

[63] J. J. Jun, N. A. Steinmetz, J. H. Siegle, D. J. Denman, M. Bauza, B. Barbarits, A. K. Lee, C. A. Anastassiou, A. Andrei, Çağatay Aydın, *et al.*, Fully integrated silicon probes for high-density recording of neural activity, Nature (London) **551**, 232 (2017).

[64] J. H. Siegle and N. A. Steinmetz, Large-scale electrophysiology at single-spike resolution, Nat. Rev. Neurosci. **27**, 395 (2026).

[65] E. Ott and T. M. Antonsen, Low dimensional behavior of large systems of globally coupled oscillators, Chaos **18**, 037113 (2008).

[66] V. V. Klinshov, D. A. Zlobin, B. S. Maryshev, and D. S. Goldobin, Effect of noise on the collective dynamics of a heterogeneous population of active rotators, Chaos **31**, 043101 (2021).

[67] R. Gămănuţ, H. Kennedy, Z. Toroczkai, M. Ercsey-Ravasz, D. C. Van Essen, K. Knoblauch, and A. Burkhalter, The mouse cortical connectome, characterized by an ultra-dense cortical graph, maintains specificity by distinct connectivity profiles, Neuron **97**, 698 (2018).

[68] J. Grandjean, A common mouse fMRI resource through unified preprocessing, Version 1, Radboud Data Repository, 2020, https://doi.org/10.34973/1he1-5c70.

[69] G. Rabuffo, J. Fousek, C. Bernard, and V. Jirsa, Neuronal cascades shape whole-brain functional dynamics at rest, eNeuro **8**, ENEURO.0283-21.2021 (2021).

[70] M. Pope, M. Fukushima, R. F. Betzel, and O. Sporns, Modular origins of high-amplitude cofluctuations in fine-scale functional connectivity dynamics, Proc. Natl. Acad. Sci. USA **118**, e2109380118 (2021).

[71] K. J. Friston, A. Mechelli, R. Turner, and C. J. Price, Nonlinear responses in fMRI: The balloon model, Volterra kernels, and other hemodynamics, NeuroImage **12**, 466 (2000).

[72] https://github.com/grabuffo/Multiscale_Brain_Criticality.